Numerical modeling of heterogeneous flow fields around rigid objects with special reference to particle paths, strain shadows and foliation drag

N. Mandal[a], S.K. Samanta[a], C. Chakraborty[b,*]

[a]Department of Geological Sciences, Jadavpur University, Calcutta 700032, India
[b]Geological Studies Unit, Indian Statistical Institute, 203, Barrackpore Trunk Road, Calcutta 700035, India

Received 2 December 1999; accepted 2 October 2000

Abstract

With the help of two-dimensional numerical models this paper investigates three aspects of heterogeneous deformation around rigid objects: (1) the nature of *particle paths*; (2) the development of *strain shadow* zones; and (3) the *drag patterns* of passive markers. In simple shear, spherical objects develop typically a concentric vortex motion, showing particle paths with an eye (double-bulge)-shaped separatrix. The separatrix has no finite dimension along the central line, parallel to the shear direction. Under a combination of pure shear and simple shear, the particle paths assume a pattern with a bow-tie shaped separatrix. With increase in the ratio of pure shear to simple shear (S_r), the separatrix around the object shrinks in size. The axial ratio of the object (R) is another important factor that controls the geometry of particle paths. When $R < 1.5$, the loci of a particle close to the object form an elliptical shell with the long axis lying along the central line. With increase in axial ratio R, the loci form a doublet elliptical shell structure. Objects with $R > 3$ do not show closed particle paths, but give rise to elliptical or circular spiral particle paths.

The development of strain shadow zones against *equant* rigid bodies depends strongly on the strain ratio S_r. When $S_r = 0$ (simple shear), they develop opposite to the extensional faces of the object, forming a typical σ-type tail. The structure has a tendency to die out with an increase in the pure shear component of the bulk deformation (S_r). The initial angle of the long axis of the object with the shear direction (ϕ) and the axial ratio of the object (R) determine the development of strain shadow zones near *inequant* rigid objects. Objects with large R and ϕ between 60 and 120° form pronounced zones of low finite strain, giving rise to strain shadow structures. A geometrical classification of diverse drag patterns of passive markers around rigid objects is presented along with their conditions of formation.

Keywords: rigid objects; Newtonian matrix; pure shear; simple shear; heterogeneous strain; Jeffery's theory

1. Introduction

Deformation of a rock system consisting of rigid objects floating in a softer matrix gives rise to a variety of geological structures, such as porphyroclast tails, inclusion trails in synkinematic porphyroblasts, strain shadows and foliation drag around large, rigid mineral grains or pebbles. All these structures are extremely useful in the kinematic analysis of deformed rocks (Spry, 1969; Rosenfeld, 1970; Willis, 1977; Simpson and Schmid, 1983; Bell, 1985; Passchier and Simpson, 1986; Ramsay and Huber, 1987; Bjornerud, 1989; Hanmer, 1990; Simpson and De Paor, 1993; Johnson and Bell, 1996). These structures

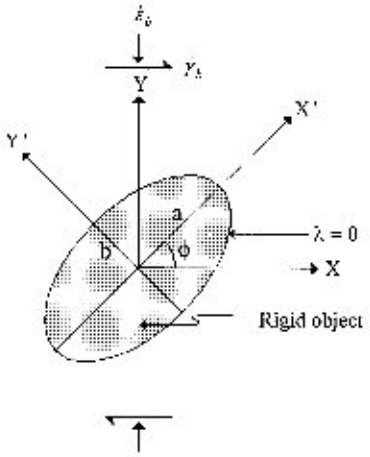

Fig. 1. Co-ordinate systems for theoretical analysis.

develop essentially in response to the instantaneous strain fields in the immediate neighborhood of an object during progressive deformation. The strain field around a rigid object is always heterogeneous (Ghosh and Ramberg, 1976; Masuda and Ando, 1988; Mandal and Chakraborty, 1990; Ildefonse and Mancktelow, 1993; ten Brink and Passchier, 1995; Masuda and Mizuno, 1996a), and the types of particle paths and deformation structures that would develop in rocks strongly depend on the nature of flow heterogeneity.

Numerical modeling based on continuum mechanics, is a convenient and useful tool for understanding the particle paths and other geological structures associated with rigid objects. For a Newtonian matrix, Lamb's (1932) theory has been utilized to model particle paths (Masuda and Ando, 1988), mantled porphyroclast systems (Bjornerud and Zhang, 1995; Masuda and Mizuno, 1996b), inclusion trail patterns of synkinematic porphyroblasts (Masuda and Mochizuki, 1989), strain shadows and drag patterns of foliation (Masuda and Ando, 1988). However, all these models apply only to spherical objects embedded in a matrix undergoing deformation either by simple shear or pure shear.

Jeffery (1922) has given an elegant mathematical treatment on the motion of ellipsoidal object embedded in a viscous medium and from his theory one can also obtain functions for the instantaneous velocity field outside the rigid object. Jezek et al. (1999) have shown that Jeffery's equations can be used for numerical modeling of heterogeneous flow around non-spherical rigid objects under deformations involving both simple and pure shear. Mandal et al. (2000) have utilized Jeffery's theory to model progressive development of mantle structures around rigid porphyroclasts in two-dimensions by considering the rigid object as an elliptical body. Following the same approach, this paper investigates the nature of particle paths, strain shadow structures and foliation drag patterns associated with equant and inequant rigid objects under different ratios of pure shear and simple shear rates in the bulk deformation.

2. Theoretical consideration

We develop numerical models in two-dimensions using the velocity field in the neighborhood of an elliptical object hosted in an infinitely extended Newtonian viscous medium following Jeffery's (1922) theory. The bulk deformation is considered to be of plane strain type with the direction of no strain at a right angle to the elliptical plane of object, which is assumed to be the axis of rigid rotation. The analysis does not take into account any effect of third dimension of the object. Let us choose a Cartesian reference frame, oxy, at the center of the object with the x-axis parallel to the bulk shear direction. The medium is subjected to a bulk deformation with a shear rate $\dot{\gamma}_b$ and a flattening rate $\dot{\epsilon}_b$, at a right angle to the shear direction. We set another reference frame, $ox'y'$, with x'-axis along the long dimension of the rigid object (Fig. 1). This reference is fixed in the object, and continuously reorients itself in the course of progressive deformation. In the foregoing analysis parameters that correspond to the $ox'y'$ coordinate system are represented by primed symbols. The position of a point near the object can be expressed by defining an elliptical coordinate system as:

$$\frac{x'^2}{a^2+\lambda} + \frac{y'^2}{b^2+\lambda} = 1 \tag{1}$$

where a and b are the major and minor semi-axes of the object. Eq. (1) implies that points with coordinates $\lambda = 0$ and ∞ lie on the surface and far away from the object, respectively. Let the long axis of the object be at angle ϕ with the bulk shear direction. At this instant the object rotates with an angular velocity ω. The velocity functions must satisfy the following boundary

conditions:

$$u'_0 = S'_{11}x' + S'_{12}y' \text{ and } v'_0 = S'_{21}x' + S'_{22}y' \quad \text{when } \lambda = \infty, \tag{2}$$

$$u'_s = -\omega y' \text{ and } v'_s = \omega x', \qquad \text{when } \lambda = 0 \tag{3}$$

S'_{ij} is the instantaneous bulk strain-rate tensor. Using the rule of tensor transformation, we have:

$$S'_{11} = \dot{\gamma}_b(S_r \cos 2\varphi + \tfrac{1}{2}\sin 2\varphi)$$

$$S'_{22} = -\dot{\gamma}_b(S_r \cos 2\varphi + \tfrac{1}{2}\sin 2\varphi)$$

$$S'_{12} = \dot{\gamma}_b(\cos^2\varphi - S_r \sin 2\varphi)$$

$$S'_{21} = -\dot{\gamma}_b(\sin^2\varphi + S_r \sin 2\varphi), \tag{4}$$

where S_r is the ratio of pure shear ($\dot{\epsilon}_b$) and simple shear ($\dot{\gamma}_b$) rates. The instantaneous velocity field in the neighborhood of the object can be described in terms of the elliptical coordinate systems in Eq. (1), and the expressions of the velocity components (derived from Eqs. (A1a) and (A1b) in Appendix A) are:

$$\begin{aligned} u' = {} & S'_{11}[1 - 2A(\alpha+\beta) + F\gamma]x' + \tfrac{1}{2}(S'_{12} + S'_{21}) \\ & \times [2(\alpha D - \beta C) + E\gamma]y' + S'_{12}y' \\ & - \frac{2\Delta x'y'}{b'^2x'^2 + a'^2y'^2}\left[\frac{1}{2}(S'_{12} + S'_{21}) \right. \\ & \times \left\{\frac{E + 2a'^2C + 2b'^2D}{a'^2}\right\}x' \\ & \left. + S'_{11}\left\{\frac{F - 2a'^2A + 2b'^2B}{b'^2}\right\}y'\right] \end{aligned} \tag{5a}$$

and

$$\begin{aligned} v' = {} & S'_{21}x' - \tfrac{1}{2}(S'_{12} + S'_{21})[2(\alpha D - \beta C) - E\gamma]x' \\ & + S'_{22}[1 - 2B(\alpha+\beta) - F\gamma]y' \\ & - \frac{2\Delta x'y'}{b'^2x'^2 + a'^2y'^2}\left[\frac{1}{2}(S'_{12} + S'_{21}) \right. \\ & \times \left\{\frac{E + 2a'^2C + 2b'^2D}{b'^2}\right\}y' \\ & \left. - S'_{11}\left\{\frac{F - 2a'^2A + 2b'^2)B}{a'^2}\right\}x'\right] \end{aligned} \tag{5b}$$

where $a' = \sqrt{a^2 + \lambda}$, $b' = \sqrt{b^2 + \lambda}$ and $\Delta = a'b'$. In such a situation α, β and γ have the following expressions:

$$\alpha = \frac{2}{(a^2 - b^2)}\left[\frac{a' - b'}{a'}\right], \tag{6a}$$

$$\beta = \frac{2}{(a^2 - b^2)}\left[\frac{a' - b'}{b'}\right], \tag{6b}$$

$$\gamma = \frac{2}{(a^2 - b^2)^2}\left[\frac{(a' - b')^2}{a'b'}\right]. \tag{6c}$$

Accordingly, the constants A–F in Eqs. (5a) and (5b) are:

$$\begin{aligned} & A = \frac{(a+b)^2}{8}, \qquad B = -\frac{(a+b)^2}{8}, \\ & C = D = \frac{ab(a+b)^2}{4(a^2+b^2)} \qquad E = -ab\frac{(a+b)^2}{2}, \\ & F = \frac{a^2+b^2}{4}(a+b)^2 \end{aligned} \tag{7}$$

The derivations of the expressions in Eqs. (6a)–(6c) and (7) are given in Appendix A. It may be noted that α, β and γ in Eqs. (6a)–(6c) tend to be zero as λ tends to infinity and Eqs. (5a) and (5b) simplify to Eq. (2). This implies that Eqs. (5a) and (5b) satisfy the boundary conditions.

Now, to find the instantaneous velocity at a point (x,y) we first perform the following coordinate transformation:

$$\begin{bmatrix} x' \\ y' \end{bmatrix} = \begin{bmatrix} \cos\varphi & \sin\varphi \\ -\sin\varphi & \cos\varphi \end{bmatrix}\begin{bmatrix} x \\ y \end{bmatrix}$$

and determine the velocity components (u',v') from Eqs. (5a) and (5b). Finally, the velocity field with respect to the fixed reference, oxy, is obtained by the

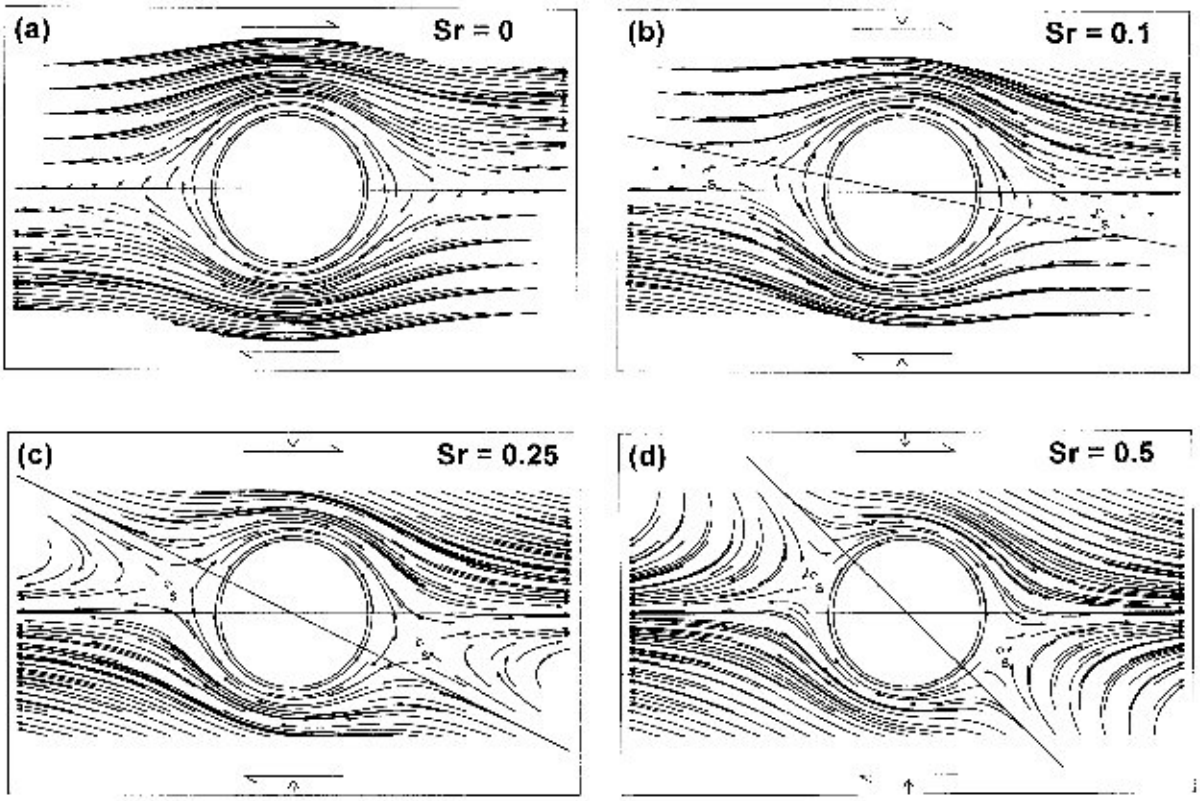

Fig. 2. Particle paths around equant rigid objects in bulk deformations with increasing ratio of pure shear to simple shear rates (S_r). (a) Simple shear. (b)–(d) Combination of pure and simple shear; straight lines parallel and inclined to the shear direction are the extensional and contractional apophyses of the bulk deformation, respectively. S: stagnation points in the flow around the rigid objects.

inverse transformation:

$$\begin{bmatrix} u \\ v \end{bmatrix} = \begin{bmatrix} \cos\varphi & -\sin\varphi \\ \sin\varphi & \cos\varphi \end{bmatrix} \begin{bmatrix} u' \\ v' \end{bmatrix} \tag{8}$$

The velocity at a point (x,y) will depend on the position of the point with respect to the object boundary. This relative position can be determined from one of the elliptical coordinates of the point, λ, which is related to the Cartesian coordinates by:

$$\lambda = \tfrac{1}{2}\Big\{(x'^2 + y'^2) - (a^2 + b^2) + \sqrt{(x'^2 + y'^2 - a^2 - b^2)^2 - 4(a^2b^2 - b^2x'^2 - a^2y'^2)}\Big\} \tag{9}$$

$\lambda > 0$ indicates a point outside the object boundary, whereas $\lambda = 0$ and $\lambda < 0$ indicate points on the surface and inside the object, respectively. At an instant, points lying outside the object will move with velocity components as in Eq. (8), while points either on the surface or inside the object will move with velocity components:

$$u = -\omega y \quad \text{and} \quad v = \omega x,$$

ω is the instantaneous angular velocity of the object, which can be obtained from Eqs. (A10) and (4) as:

$$\omega = -\frac{a^2(\dot{\gamma}_b \sin^2\varphi + \dot{\epsilon}_b \sin 2\varphi) + b^2(\dot{\gamma}_b \cos^2\varphi - \dot{\epsilon}_b \sin 2\varphi)}{a^2 + b^2} \tag{10}$$

3. Numerical simulation

The heterogeneous deformations of the matrix material around a rigid object were analyzed by considering incremental displacements of material points during

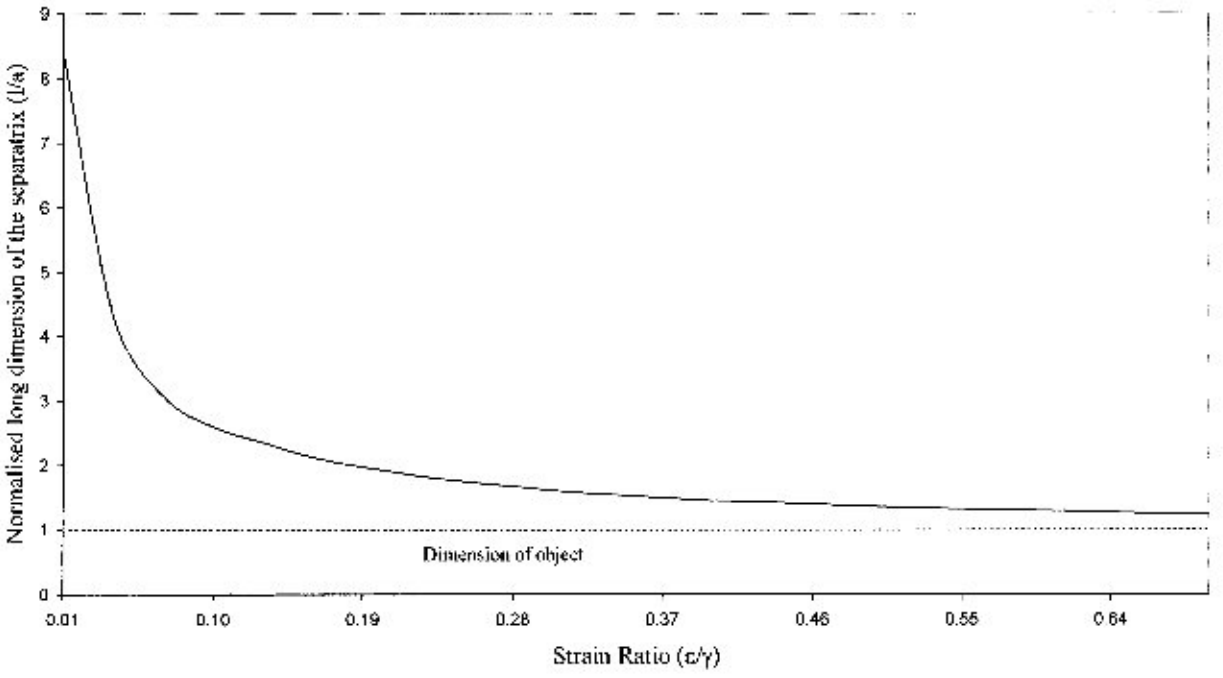

Fig. 3. Variation in the long dimension of separatrix (radial distance of stagnation points), normalized to object's dimension, a, with increase in the ratio of pure shear and simple shear rates (S_r).

progressive deformation. Let the position of a point is (x_i, y_i) at the ith increment; the point is displaced during an incremental time interval δt:

$$x_{i+1} = x_i + u_i\,\delta t$$

$$y_{i+1} = y_i + v_i\,\delta t$$

u_i and v_i are the velocity components at the ith increment. During this incremental deformation the object rotates to a new position, and so does the reference frame to remain in coincidence with the axial directions of the object. The new position of the reference is: $\phi_{i+1} = \phi_i + \omega_i\,\delta t$, where ω_i is instantaneous velocity of the object at ith increment (Eq. (10)). In the next increment, i.e. $(i+1)$th increment, the displacement of the point is calculated by taking the new position of the point with respect to the object. We ran numerical model experiments for a large number of increments using Microsoft Visual Basic computer software.

3.1. Particle paths

In order to characterize the heterogeneous flow fields around a rigid object during deformation it is essential to describe the possible patterns of particle paths under varying conditions of deformation (e.g. Ramberg, 1975). In rotational deformations the presence of a spherical rigid object induces concentric particle paths in the surrounding matrix. Two types of paths have been predicted — one with eye-shaped separatrix and the other with bow-tie shaped separatrix, which develop in Newtonian and non-Newtonian matrix, respectively (Passchier, 1994). Masuda and Mizuno (1996a,b), however, have shown that the flow with double-bulge shaped (i.e. eye-shaped) separatrix may develop in both the rheological varieties. Recently, Pennacchioni et al. (2000), on the other hand, have proposed that bow-tie-shaped separatrix develop under simple shear irrespective of matrix rheology. Our analysis reveals that the geometry of particle paths are sensitive to the shape of rigid objects ($R = a/b$) and the ratio of pure shear and simple shear rates (S_r) in the bulk deformation, and describes some new types of particle paths around inequant objects.

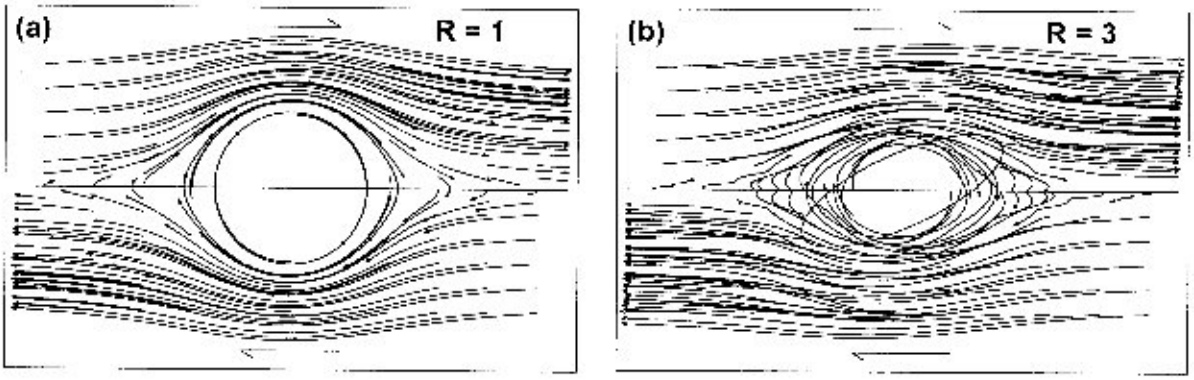

Fig. 4. Flow patterns around: (a) equant, and (b) inequant rigid objects. In (b) the long axis of the object was initially parallel to the shear direction. R: axial ratio of the object.

3.1.1. Influence of the strain ratio (S_r)

A set of numerical simulations was performed with equant objects ($R = 1$) under different ratios of pure shear and simple shear rates (S_r) in the bulk deformation. When $S_r = 0$, the object induced particle paths with a typical eye-shaped separatrix (Fig. 2a). The separatrix has a finite dimension across its longer direction, but becomes asymptotic along the length (Fig. 2a, cf. Masuda and Mizuno, 1996a). The absence of stagnation points (zero velocity) is a characteristic feature of the flow pattern around the object. When S_r is increased the separatrix becomes finite both along and across its length and two diametrically opposite stagnation points appear (Fig. 2b). With further increase in S_r, particle paths in the immediate neighborhood of the object become elliptical and those away from the object are hyperbolic. The separatrix of the two types of paths assumes a bow-tie shaped geometry (Fig. 2c). The line joining the stagnation points bisects the extensional and contractional apophyses of bulk deformation (Fig. 2c). The distance between the stagnation points determines the longer dimension of the separatrix. When S_r is very large (≈ 0.5), the separatrix shrinks in size and becomes more equant, as the stagnation points shift close to the object (Figs. 2d and 3).

To summarize, the flow pattern around an equant rigid object in simple shear is characterized by a semi-infinite eye-shaped separatrix, which in bulk deformations by a combination of simple shear and pure shear assumes a bow-tie shaped geometry with finite dimensions. The inclination of the longer dimension of a finite separatrix with the bulk shear direction can be given by:

$$\theta = -\tfrac{1}{2}\tan^{-1}(2S_r). \tag{11}$$

Eq. (11) shows that the long axis of the separatrix will be parallel to the shear direction when the bulk deformation is under simple shear ($S_r = 0$), as seen in earlier models (Masuda and Mizuno, 1996a; Passchier, 1994). In general deformations ($S_r \neq 0$) the long axis is at an angle with the shear direction and the inclination will be close to 135° when S_r is very large.

3.1.2. Influence of the shape of the rigid object

Numerical models with inequant objects show more complex particle paths than those in models with equant objects. The paths are mutually disharmonic, and intersect one another, implying an unsteady flow around the object. In case of equant objects, each particle lying between the separatrix and the surface of the object moves along a closed path and reverses its movement direction twice. The points of reversals lie on the central shear plane, diametrically opposite to each other (Fig. 4a). In contrast, a particle in the vicinity of an inequant object reverses the movement direction several times while moving along closed paths (Fig. 4b). The reversal points are generally located away from the central shear plane.

Numerical models reveal that the trajectory of a particle close to the object is sensitive to its axial

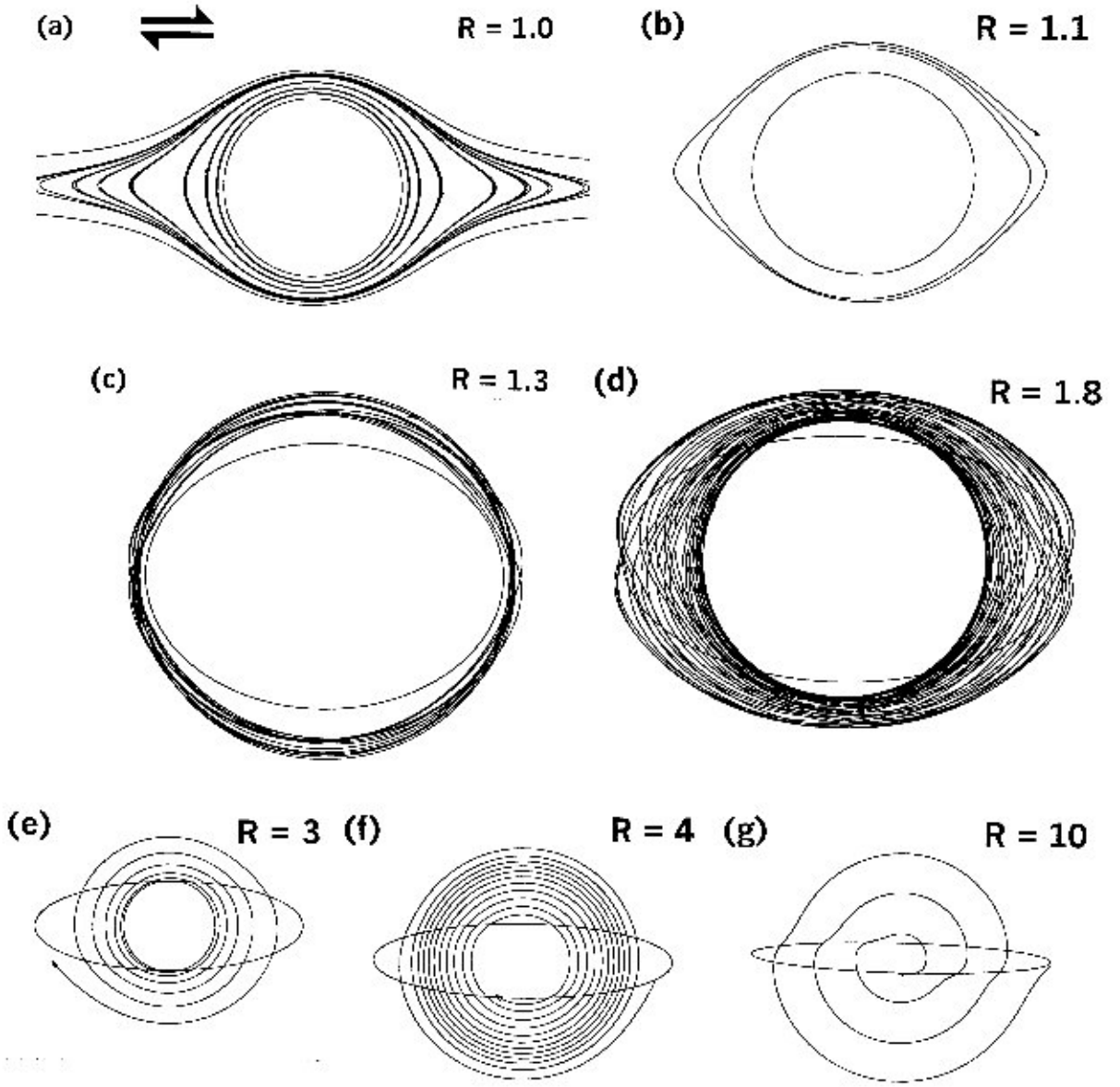

Fig. 5. Loci of a particle (s) controlled by the axial ratio (R) of rigid object. (a) Individual particles tracking repeated elliptical paths. (b) Loci of a particle forming an elliptically spiral path. (c) Particle path around an inequant object defining a shell. (d) Particle path defining a doublet shell (see text for details). (e) and (f) Outward- and inward-spiraling paths of a particle initially located near the extensional and contractional faces of inequant objects, respectively. (g) Distorted spiral path of a particle initially located near the tip of the object. R: axial ratio of the rigid objects. It may be noted that the objects shown in the figures are in their initial positions.

ratio, R. When the object is equant ($R = 1$), the particle tracks a single closed, elliptical path throughout progressive deformation (Fig. 5a). With a slight departure from the equant shape ($R = 1.1$), the particle tracks an elliptically spiral path (Fig. 5b). During progressive shear the spiraling particle executes alternate outward and inward movement with respect to the center of the rigid object with a periodicity (Fig. 5c). However, the outward and inward movement remains confined within a specified zone

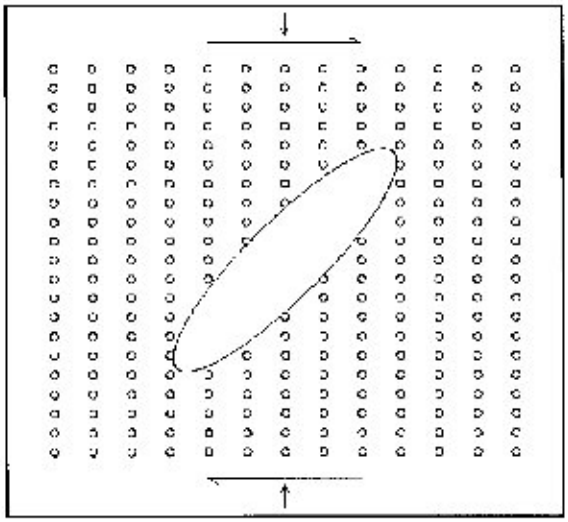

Fig. 6. Initial model with circular strain markers in a Cartesian grid around a rigid object to be deformed under varying ratios of pure shear and simple shear rates.

surrounding the object forming a kind of shell structure around the object (Fig. 5c). The shell geometry is simple when the axial ratio of the object is small ($R = 1.3$, Fig. 5c) but assumes a complex, doublet configuration for larger values of axial ratio ($R = 1.5$, Fig. 5d).

Particles do not follow closed paths, or define shell structures, when the axial ratio of the object is larger ($R > 3$). In the close vicinity of the object they track more or less harmonic oval or circular spiral paths (Fig. 5e and f). Two types of spiral paths are recognized: *cyclone* (Fig. 5e) and *anticyclone* (Fig. 5f) paths defining continuous outward and inward movement, respectively, depending on the position of the particle. Particles with their initial position near the surface of object in the extensional field show cyclonic, those at the other side anti-cyclonic movement. The first path type indicates that a line can undergo continuous stretching in progressive shear. This is in contrast to the cases the lines were alternately shortened and extended, defining a pulsating deformation (Ramberg, 1975). With further increase in axial ratio of the object, a different type of particle kinematics is noticed. Particles near the tip of an object with $R = 10$ move inward following alternately circular and curvilinear paths, giving rise to distorted spiral paths (Fig. 5g).

3.2. Strain shadow zones around rigid objects

The development of strain shadow zones around rigid mineral grains or pebbles is clearly manifested in the preferential localization of equant quartz grains surrounding the rigid object in many naturally deformed rocks (Spry, 1969; Ramsay and Huber, 1987). This work analyzes what controls the development of strain shadow zones around rigid objects and describes their morphologies.

The strain distribution patterns around rigid objects can be visualized by analyzing the deformation of numerous, small, initially circular markers, distributed around the object at an equal spacing in a Cartesian grid (Fig. 6). The strain shadow zones were defined as zones where the ratio of local and far-field finite strains was less than 0.5. The development and distribution of strain shadow zones were investigated with the help of numerical models involving three principal variables: (1) the ratio of pure shear and simple shear rates in the bulk deformation (S_r); (2) the axial ratio of object (R); and (3) the initial orientation of the long axis of object with the shear direction (ϕ).

3.2.1. Influence of the strain ratio (S_r)

A set of simulations was performed with equant rigid objects under different values of S_r. When $S_r = 0$, strain shadow domains develop against the two extensional faces of the object describing a σ-type geometry (Fig. 7a). The zones of high strain occur near the contraction face of the object and along long bands at an angle less than 45° with the shear direction (Fig. 7a and b, cf. Masuda and Ando, 1988). The low-strain zones tend to shrink, as S_r is increased (Fig. 7b and c), and when the deformation is entirely by pure shear no strain shadow zone occurs as defined in the present study (Fig. 7d).

The effect of S_r on the development of strain shadow structures can also be understood by the strain path of a particular material point in the neighborhood of the object. For low values of S_r (0–0.5), the finite strain of a material point initially located near the contractional face of the object increases to a maximum and then decreases with progressive increase in finite bulk shear (Fig. 8). Upon increasing the value of S_r (>1), the finite strain of the material point, on the other hand, continues to increase with increasing bulk

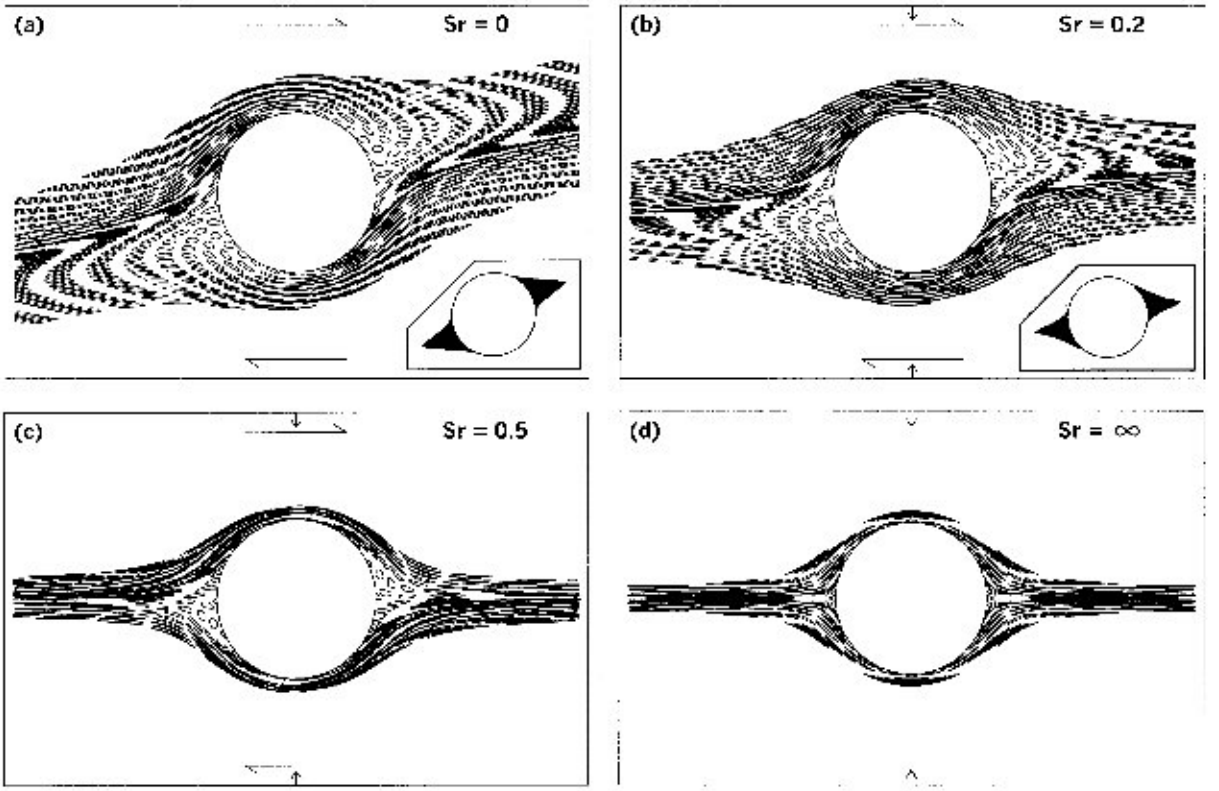

Fig. 7. Strain distributions around equant ($R = 1$) rigid objects for different ratios of pure and simple shear rates (S_r). Finite bulk shear = 4.0. Strain shadow zones (shaded) are shown in insets.

shear (Fig. 8). This again implies that strain shadows would be prevalent where simple shear component dominates in the bulk deformation, and that material points defining a high-strain zone at one moment may enter a zone of strain shadow in the course of progressive deformation at low values of S_r.

3.2.2. Strain shadow around inequant objects

Numerical simulations were made under simple shear by varying the initial axial orientation of the object with respect to the shear direction (ϕ) and the axial ratio of the object (R). Strain shadow zones form when the long axis of the object makes an angle between 60 and 135° with the shear direction (Fig. 9). When ϕ is close to 60°, the strain shadow zone forms a narrow tail, emerging from the tip of the object (Fig. 9a). With increase in inclination, the shadow zone becomes wider and longer (Fig. 9b), and at $\phi = 120°$, they form bands giving rise to an overall pattern similar to that of augen structures (Fig. 9c). The low-strain zones die out as the inclination of the object is further increased (Fig. 9d) and instead a narrow zone of strong strain concentration appears sub-parallel to the long axis of object (Fig. 9d).

For a given ϕ, with increase in axial ratio of the rigid object strain shadow zones progressively increase in length as well as change their pattern (Fig. 10). When the axial ratio is low ($R = 1.5$), the strain shadow zones resemble σ-type tails emerging from the nodes of the object. With increase in axial ratio, R, the zone forms wings, which finally form a band surrounding the object (Fig. 10d).

3.3. Distortion patterns of passive markers

3.3.1. Initial model

Numerical models initially had a set of parallel marker lines at an angle θ with the shear direction.

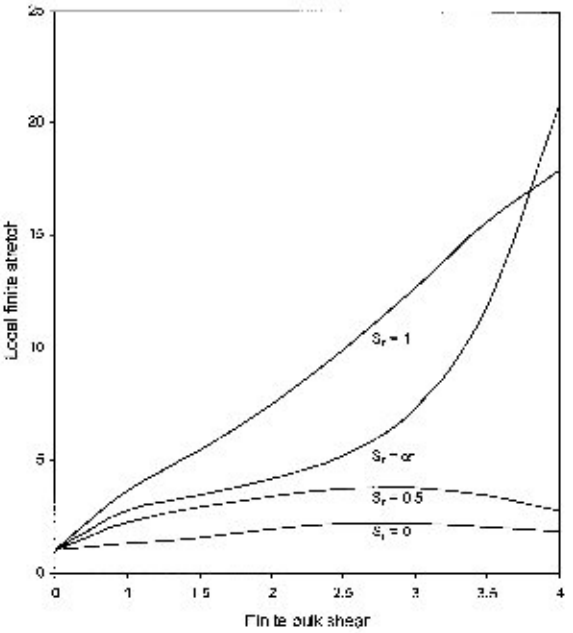

Fig. 8. Strain paths at a point initially located near the contractional face of an equant object in progressive deformation under different ratios of pure and simple shear rates (S_r).

A line in xy-space can be represented by:

$$x \sin \theta - y \cos \theta - p = 0,$$

where p is the *normal* distance of a line from the center of the object. The distortion pattern of a line was simulated numerically from incremental displacement (Eq. (8)) of equally spaced points on the line. Three factors — (1) the initial orientation of marker line (θ), (2) the axial ratio of object (R) and (3) the strain ratio (S_r) in bulk deformation, were taken into account in the simulations. For convenience, we first classify the drag patterns, which were obtained by varying the above three parameters.

3.3.2. Types of drag patterns

Type 1: Markers form bi-convex curvatures around the object (Fig. 11). Type 2: Markers are distorted in the form of folds on either side of the object (Fig.11a). Depending upon the degree of relative curvature, the drag folds can again be classified into three sub types: Types 2a–2c. The first two types are characterized by larger curvatures of folds with inward convexity, and they differ from each other by the opposite sense of arrangement of folds with inward and outward curvatures. Type 2c has drag folds with outward

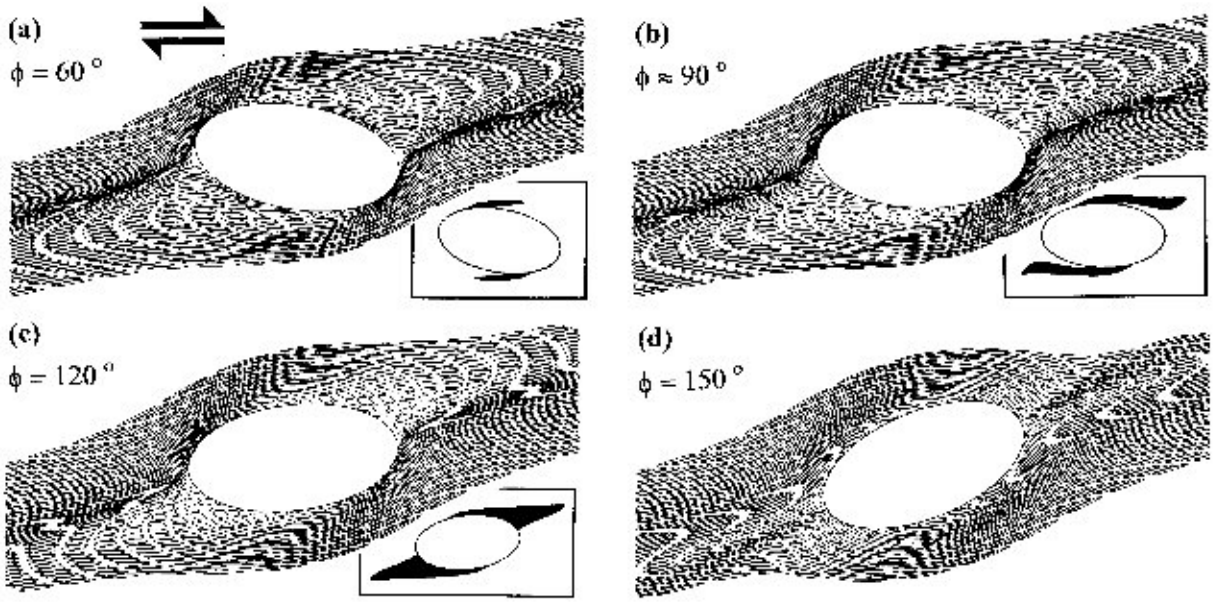

Fig. 9. Strain distributions around inequant objects ($R = 2$) with different initial inclinations of their long axes to the shear direction (ϕ) Finite bulk shear = 4.0. Strain shadow zones (shaded) are shown in insets.

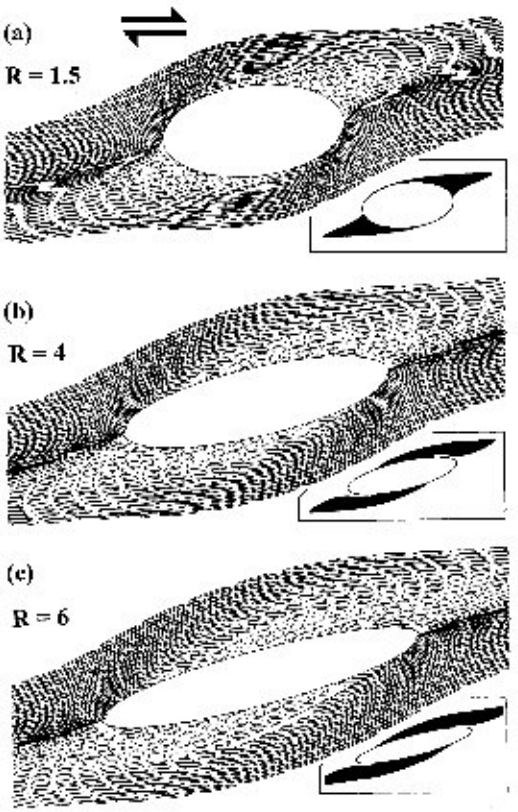

Fig. 10. Strain shadow patterns near inequant objects of different axial ratios (R). The long axis of the objects was initially at an angle $\phi = 120°$ with the shear direction.

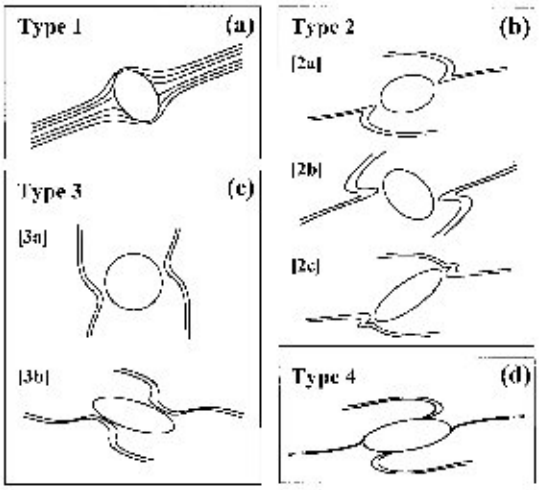

Fig. 11. Types of drag patterns obtained from numerical simulations (see text for details).

convex curvatures much greater than inward convex curvatures. Type 3: Markers are distorted with inward convex curvatures, giving rise to a geometry very similar to that of the millipede structures of Bell and Rubenach (1980). They have either smooth, rounded (single-hinged) (Type 3a) or flat (double-hinged) (Type 3b) crests (Fig. 11c). Type 4: The drag effect of object is such that the markers are distorted in the form of overturned folds on either face of the object (Fig. 11d). This type of drag patterns has been produced in analog model experiments (Van Den Driessche and Brun, 1987).

3.3.3. Drag patterns around equant objects

Earlier workers have shown that the initial orientation of passive markers is a controlling factor in the development of different types of drag patterns around spherical rigid objects (Ghosh, 1975; Masuda and Ando, 1988). In this section we present some details of the distortion patterns revealed in our numerical models by varying the initial orientation of markers at different ratios of pure shear and simple shear rates in the bulk deformation (S_r).

For $S_r = 0$, markers with an initial inclination θ between 0 and $-45°$ developed Type 2 drag folds (Fig. 12a), as in analog model experiments (Ghosh, 1975) and earlier numerical simulations (Masuda and Ando, 1988). For any other orientations they produced Type 1 — distortion patterns (Fig. 12a), which are frequently noticed around rigid objects in deformed foliated rocks. Markers at a low angle to the shear direction produced Type 2a fold pattern, which is replaced by Type 2b when θ is between -20 and $-45°$ (Fig. 12a; cf. Masuda and Ando, 1988). The axial traces of inwardly convex folds on either side of the object in both the Types 2a and 2b patterns show a side stepping with the sense in consistence with that of bulk shear (Fig. 12a).

Under a combination of pure shear and simple shear, the strain ratio S_r influences mainly Type 2 drags (Fig. 12b). With increase in S_r, Type 2a folds tend to die out, whereas Type 2b folds are progressively accentuated (Fig. 12a and b).

3.3.4. Drag patterns around inequant objects

Each of the three factors mentioned earlier was

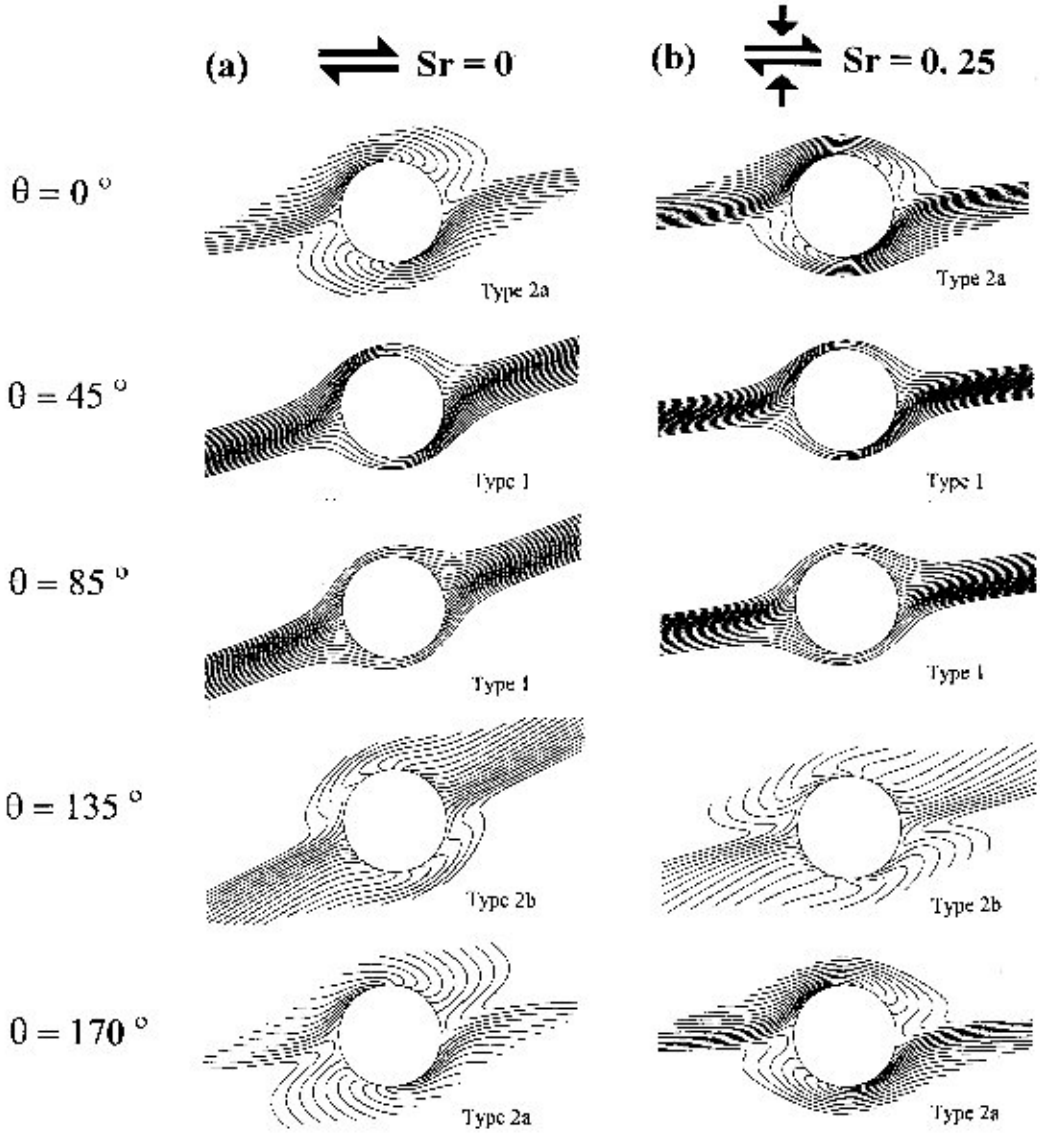

Fig. 12. Distortion patterns of marker lines around equant rigid objects. θ is the initial inclination of marker with the shear direction. (a) Simple shear. (b) Combination of pure and simple shears. S_r is the ratio of pure to simple shear rates.

varied independently in different sets of numerical simulations with inequant objects. We discuss the results separately in the following paragraphs. The simulations were performed under simple shear, i.e. $S_r = 0$.

(1) The axial ratio of object was varied, keeping the passive markers and the long axis of object parallel to the shear direction. Objects with $R = 1.5$ developed Type 2a folds (Fig. 13a). With increase in R, the inward curvatures tend to have a double-hinged geometry, giving rise to a Type 3b pattern that resembles millipede structures. The other types of drag pattern did not change significantly with increase in axial ratio of the object.

(2) The inclination of the long axis of object with the shear direction (ϕ) was varied, keeping markers parallel to the shear direction. When ϕ is between 45

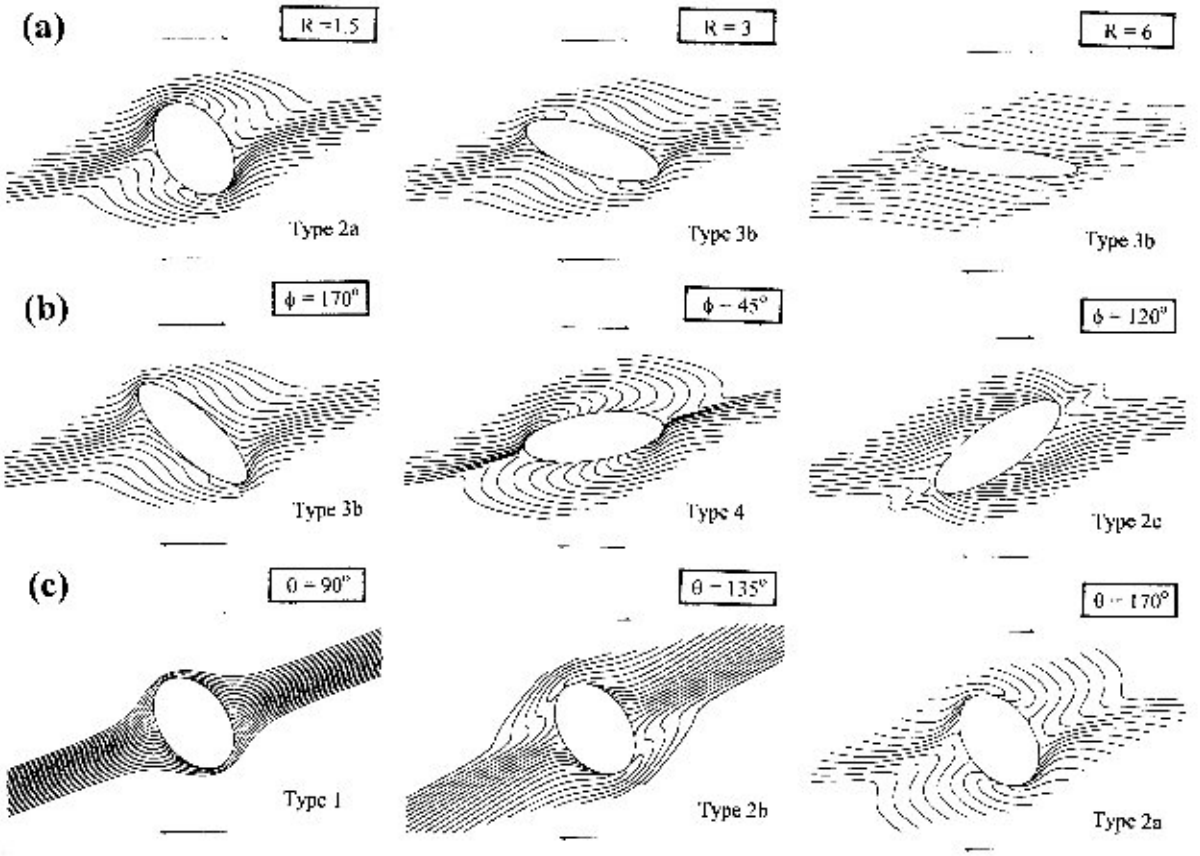

Fig. 13. Drag patterns of marker lines around inequant objects. (a) R was varied, keeping $\theta = 0$ and $\phi = 0$. (b) ϕ was varied, keeping $R = 3$ and $\theta = 0$. (c) θ was varied, keeping $R = 1.5$ and $\phi = 0$. In all the cases $S_r = 0$. R: axial ratio of object; ϕ: initial inclination of the long axis of object with the shear direction; θ: initial inclination of marker with the shear direction.

and −45°, Type 3 drag folds form (Fig. 13b). This drag pattern is replaced by Type 4 when ϕ is larger than 45° but less than 90°. For $\phi > 90°$, this drag geometry assumes the Type 2c pattern, characterized by outward convex curvature, which is higher than the inward convex curvatures.

(3) The initial inclination of marker, θ, was varied, keeping the long axis of object parallel to the shear direction. For θ around 90°, the markers bowing around the object are distorted with a Type 1 pattern, whereas those abutting against the object show a transition between normal and reverse drags (Fig. 13c). The points, where this transition occurs, show a sidestepping with respect to the general trend of the markers, and the sense of sidestepping is consistent with the bulk shear sense (Fig. 14). With increase in θ Type 2b patterns appear at around $\theta = 120°$, which is replaced by Type 2a pattern at around $\theta = 170°$.

4. Summary

The principal factors governing the nature of heterogeneous deformation around rigid objects floating in a Newtonian matrix are: (1) the axial ratio (R) and the initial orientation (ϕ) of the long axis of the object; (2) the initial orientation (θ) of markers showing distortion patterns; and (3) the ratio (S_r) of pure shear and simple shear rates in the bulk deformation.

Equant objects perturb simple shear flow in the matrix forming vortex motion with eye-shaped separatrix, as

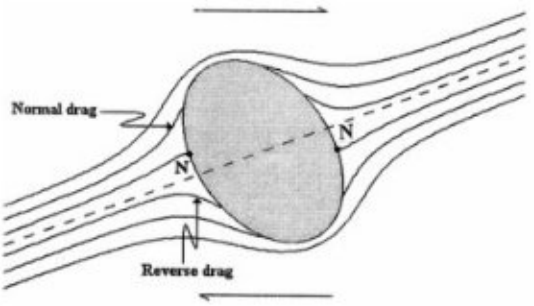

Fig. 14. Transition between normal and reverse drags along the surface of object. N is the null point marking the transition.

shown by Passchier (1994) and Masuda and Mizuno (1996a,b). The separatrix turns into a bow-tie shape when the bulk deformation takes place by a combination of simple shear and pure shear. The long dimension of the separatrix is inversely proportional to the strain ratio S_r (Fig. 3). The numerical analysis reveals some new types of particle paths associated with inequant objects. For a slight departure from the equant shape of object, particles do not track single close paths, but show loci forming an elliptical shell about the object. Objects with axial ratio between 2 and 3 show pulsating movement of particles along differently oriented close paths forming doublet elliptical shell structure. Objects with large axial ratios ($R > 3$) perturb the flow resulting in elliptically or circularly spiral inward or outward motion of particles.

Rigid mineral grains or porphyroblasts are often associated with strain shadow zones in their neighborhood forming tails of segregated minerals, like quartz. Our numerical models suggest that, if the rigid objects have a coherent interface with the matrix, strain shadow zones can develop only when the ratio of pure shear and simple shear rates in the bulk deformation is low. The analysis refines earlier numerical studies (Masuda and

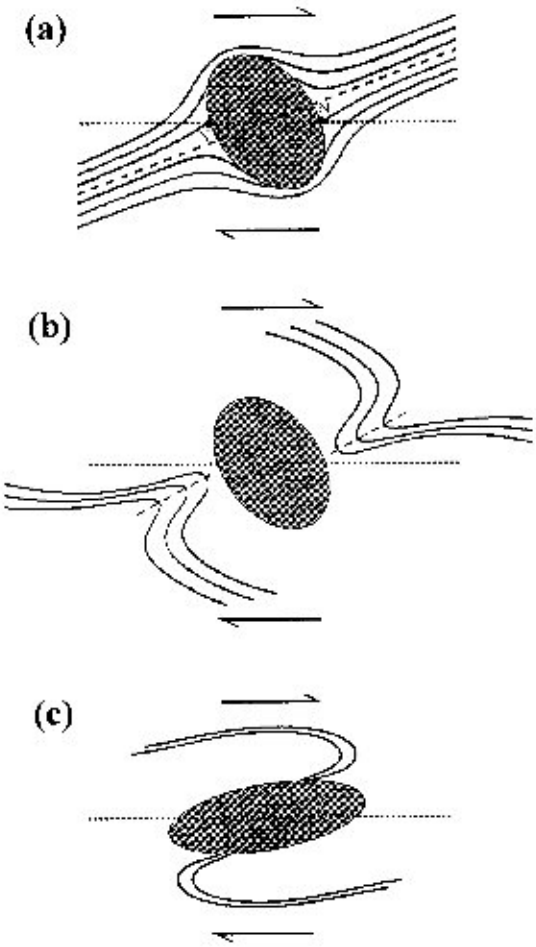

Fig. 15. Drag patterns as shear sense indicators. (a) Sidestepping of null points (N) separating normal and reverse drags. (b) Sidestepping of axial traces (dashed line) of inwardly convex drags. (c) Vergence of overturned drag folds on the long faces of objects with a large axial ratio.

Table 1
Fields of different types of drag patterns around inequant rigid objects ($R = 3$) in the $\phi - \theta$ space

Inclination of marker (θ)	Inclination of long axis of object (ϕ)				
	0	45	90	135	180
0	Type 3b	Type 4	Type 4	Type 2c	Type 3b
45	Type 1	Type 1	Type 4	Type 1	Type 1
90	Type 1	Type 1	Type 1	Type 1	Type 1
135	Type 2c	Type 2b	Type 3a	Type 3b	Type 2c
180	Type 3b	Type 4	Type 4	Type 2c	Type 3b

Ando, 1988; Masuda and Mizuno, 1996a,b) by incorporating the shape and initial orientation of the object as additional controlling factors. Low-strain zones develop if the initial inclination of the long axis of the object with the shear direction lies between 60 and 135°, and the zones tend to be more and more prominent as the axial ratio of object is increased.

Analog model experiments (Ghosh and Ramberg, 1976) have revealed different drag patterns around elongate rigid objects. The analyses are, however, limited to moderate bulk strain. Numerical simulations of Masuda and Ando (1988) indicate that complex drag patterns may develop during a large strain. Our study presents the probable drag patterns around elongate rigid bodies at a large bulk strain. The patterns are classified broadly into four types (Fig. 11). Table 1 summarizes the conditions at which different types of drag patterns develop, as revealed from the numerical models. Our simulations reveal that Types 2c, 3b and 4 develop around inequant objects under specific conditions, whereas rest of the types is common to both equant and inequant objects.

Some of the features in the drag patterns discussed above can be used in determining the sense of bulk shear: (1) shifting of null points separating normal and reverse drags from the general trend of foliation in Type 1 distortion patterns (Fig. 15a), (2) sidestepping of the axial traces of inwardly convex drag in Type 2 patterns (Fig. 15b), and (3) vergence of overturned drag folds in Type 4 patterns, (Fig. 15c).

The principal limitations that adhere to the present model are: (1) The analysis is two-dimensional, and based on the assumptions of plane strain type of bulk deformation and elliptical rigid object instead of an ellipsoidal body. However, some of our numerical simulations (e.g. particle paths, distortion patterns of passive markers) conform to that obtained from 3D considerations (Jezek et al., 1999) of Jeffery's theory (1922) that satisfy Stoke's equations for viscous flow. (2) The rotation axis of the rigid object is assumed to remain always in coincidence with the direction of no-strain. The numerical modeling of heterogeneous deformation involving rigid rotation in a 3D space would be much more complicated than that presented in this paper, and the application of special computer software would be necessary, as shown by Jezek et al. (1999). (3) The matrix is assumed to be of Newtonian rheology, and does not experience any volume change during the deformation.

Acknowledgements

We wish to thank Drs G. Oertel and J. Jezek for their critical comments and suggestions. The present work was carried out under a project of DST, India sanctioned to N.M. C.C acknowledges the infrastructural facilities provided by the Indian Statistical Institute, Calcutta.

Appendix A

This section presents mathematical details of the velocity functions (Eqs. (5a) and (5b)), based on which the numerical experiments were performed. We follow Jeffery's (1922) mathematical procedure in expressing the velocity functions outside an elongate rigid object floating in a Newtonian matrix of infinite extension. Jeffery has presented the mathematical formulation for the velocity field in three dimensions. His final equations (Eqs. 22 and 23) basically represent converging functions, which tend to have finite values at a large distance from the object. In analogy with this approach, we consider Jeffery's differential equations (Eqs. 18 and 19) of the velocity field in two-dimension satisfying the condition of continuity, and obtained similar velocity functions for our 2D model, assuming that the bulk deformation is of plane strain type and the rigid object is an ellipse with its rotation axis along the direction of no-strain. Under this condition, the expressions of velocity components are obtained as follows:

$$u' = [S'_{11} - 2A_1(\alpha + \beta) - F_1\gamma]x' + [S'_{12} - 2 \times(\alpha D_1 - \beta C_1) + E_1\gamma]y' - \frac{2x'P^2}{(a+\lambda)\Delta}\left[\{E_1 + 2 \times(a^2+\lambda)C_1 + 2(b^2+\lambda)D_1\}\frac{1}{(a^2+\lambda)(b^2+\lambda)}x'y'\right] - \frac{2x'P^2}{(a+\lambda)\Delta}\left[\{F_1 - 2(a^2+\lambda)A_1 + 2(b^2+\lambda)B_1\}\frac{1}{(b^2+\lambda)^2}y'^2\right] \quad \text{(A1a)}$$

$$v' = [S'_{22} - 2B_1(\alpha + \beta) - F_1\gamma]y' + [S'_{21} - 2(\alpha D_1 - \beta C_1) + E_1\gamma]x' - \frac{2y'P^2}{(b^2+\lambda)\Delta}\left[\{E_1 + 2(a^2 + \lambda)C_1 + 2(b^2+\lambda)D_1\}\frac{1}{(a^2+\lambda)(b^2+\lambda)}x'y'\right] + \frac{2y'P^2}{(b^2+\lambda)\Delta}\left[\{F_1 - 2(a^2+\lambda)A_1 + 2(b^2+\lambda)B_1\}\frac{1}{(a^2+\lambda)^2}x'^2\right] \quad \text{(A1b)}$$

where

$$\frac{1}{P^2} = \frac{x'^2}{(a^2+\lambda)^2} + \frac{y'^2}{(b^2+\lambda)^2}.$$

A_1–F_1 in Eqs. (A1a) and (A1b) are constants; these are indexed to distinguish from the constants A–F in Eqs. (5a) and (5b). The constants are comparable, respectively, with A, B, H, H', T, W in Eqs. (22) and (23) of Jeffery (1922), the expressions of which have been given in Eqs. (25)–(27). We, however, derive the expressions of these constants independently because the velocity functions in our case are written in two-dimensions. α, β and γ are elliptic integrals that can be expressed as (cf. Eqs. (9)–(11) of Jeffery 1922):

$$\alpha = \int_\lambda^\infty \frac{d\lambda}{(a^2+\lambda)\Delta}, \quad \text{(A2a)}$$

$$\beta = \int_\lambda^\infty \frac{d\lambda}{(b^2+\lambda)\Delta} \quad \text{(A2b)}$$

$$\gamma = \int_\lambda^\infty \frac{d\lambda}{(a^2+\lambda)(b^2+\lambda)\Delta}, \quad \text{(A2c)}$$

where Δ is a geometrical parameter that relates to the geometrical dimension of the medium enclosed within a λ contour. In Jeffery (1922) this parameter is a measure of an ellipsoidal volume of the medium around the rigid object. As our analysis is restricted to two-dimension, we take the parameter as a measure of area represented by a concentric elliptic contour around the elliptical object. Thus, whereas Jeffery expresses Δ as $\sqrt{(a^2+\lambda)(b^2+\lambda)(c^2+\lambda)}$, we express it as: $\Delta = \sqrt{(a^2+\lambda)(b^2+\lambda)}$. Substituting this expression of Δ, the integration in Eq. (A2a) can be solved along the following steps:

$$\int \frac{d\lambda}{(a^2+\lambda)\Delta}$$

$$\Rightarrow \int \frac{d\lambda}{(a^2+\lambda)^{3/2}(b^2+\lambda)^{1/2}}$$

Let us put $Z = \sqrt{b^2+\lambda}$. Then $d\lambda = 2Z\,dz$ and the integration is rewritten as:

$$\Rightarrow \int \frac{2dZ}{(A^2+Z^2)^{3/2}}$$

where $A^2 = a^2 - b^2$.We again replace by $Z = A\tan\theta$, which after differentiation gives, $dz = A\sec^2\theta\,d\theta$, and get

$$\Rightarrow \int \frac{2A\sec^2\theta\,d\theta}{(A^2 + A^2\tan^2\theta)^{3/2}}$$

After simplification we have:

$$\Rightarrow \frac{2}{A^2}\int \cos\theta\,d\theta$$

$$\Rightarrow \frac{2}{A^2}\sqrt{\frac{Z^2}{A^2+Z^2}}.$$

After replacing Z^2 by $b^2+\lambda$ and A^2 by a^2-b^2, we can now get the solution of definite integral in Eq. (A2a) as:

$$\alpha = \frac{2}{a^2-b^2}\left[\frac{\sqrt{b^2+\lambda}}{\sqrt{a^2+\lambda}}\right]_\lambda^\infty$$

$$\alpha = \frac{2}{a^2-b^2}\left[\frac{\sqrt{a^2+\lambda}-\sqrt{b^2+\lambda}}{\sqrt{a^2+\lambda}}\right] \quad \text{(A3)}$$

The expression of β in Eq. (A2b) can be obtained by solving the integral in the same way as:

$$\beta = \frac{2}{a^2-b^2}\left[\frac{\sqrt{a^2+\lambda}-\sqrt{b^2+\lambda}}{\sqrt{b^2+\lambda}}\right]. \quad \text{(A4)}$$

In order to find the expression of γ, we solve the integration in Eq. (A2c) along the following steps:

$$\int \frac{d\lambda}{(a^2+\lambda)(b^2+\lambda)\Delta}$$

$$\Rightarrow \int \frac{dZ}{Z^2(A^2+Z^2)^{3/2}},$$

where $Z=\sqrt{b^2+\lambda}$ and $A^2=a^2-b^2$.

$$\Rightarrow \frac{2}{A^4}\int \frac{d\theta}{\tan^2\theta\sec\theta},$$

where $Z=A\tan\theta$

$$\Rightarrow \frac{2}{A^4}\int \frac{\cot^2\theta\, d\theta}{\sec\theta}$$

$$\Rightarrow \frac{2}{A^4}\int\left(-\cos\theta+\frac{\cos^2\theta}{\sin^2\theta}\right)d\theta$$

$$\Rightarrow -\frac{2}{A^4}\left[\frac{\sqrt{b^2+\lambda}}{\sqrt{a^2+\lambda}}+\frac{\sqrt{a^2+\lambda}}{\sqrt{b^2+\lambda}}\right].$$

The expression of γ then follows:

$$\gamma=-\frac{2}{(a^2-b^2)^2}\left[\frac{\sqrt{b^2+\lambda}}{\sqrt{a^2+\lambda}}+\frac{\sqrt{a^2+\lambda}}{\sqrt{b^2+\lambda}}\right]_\lambda^\infty$$

$$\Rightarrow \gamma=\frac{2}{(a^2-b^2)^2}\left[\frac{\left(\sqrt{a^2+\lambda}-\sqrt{b^2+\lambda}\right)^2}{\sqrt{a^2+\lambda}\sqrt{b^2+\lambda}}\right] \quad \text{(A5)}$$

Eqs. (A1a) and (A1b) contain six unknowns, which can be determined by imposing boundary conditions. If the instantaneous rotation rate of the object is ω, the velocity of a point on the surface of object, $\lambda=0$ will be:

$$u'_s=-\omega y' \text{ and } v'_s=\omega x' \quad \text{(A6)}$$

Substituting $\lambda=0$ in Eqs. (A1a) and (A1b) and comparing them with those in Eq. (A6), the following equations can be formed:

$$S'_{11}+F_1\gamma-2A_1(\alpha_o+\beta_o)=0 \quad \text{(A7a)}$$

$$S'_{12}+E_1\gamma+2(\alpha_oD_1-\beta_oC_1)=-\omega \quad \text{(A7b)}$$

$$E_1+2a^2C_1+2b^2D_1=0 \quad \text{(A7c)}$$

$$F_1-2a^2A_1+2b^2B_1=0 \quad \text{(A7d)}$$

$$S'_{21}+E_1\gamma_o-2(\alpha_oD_1-\beta_oC_1)=\omega \quad \text{(A7e)}$$

$$S'_{22}-F_1\gamma_o-2B_1(\alpha_o+\beta_o)=0 \quad \text{(A7f)}$$

Now, solving these six Eqs. (A7a)–(A7f) the coefficients are obtained in terms of known quantities.

$$\left.\begin{aligned}
A_1&=\frac{S'_{11}}{2[(\alpha_o+\beta_o)-(a^2+b^2)\gamma_o]},\\
B_1&=\frac{S'_{22}}{2[(\alpha_o+\beta_o)-(a^2+b^2)\gamma_o]},\\
C_1&=\frac{\frac{1}{2}\alpha_o(S'_{21}+S'_{12})-\gamma_ob^2(\frac{1}{2}(S'_{21}-S'_{12})-\omega)}{2(\alpha_oa^2+\beta_ob^2)\gamma_o}\\
D_1&=\frac{\frac{1}{2}\beta_o(S'_{21}+S'_{12})+\gamma_oa^2(\frac{1}{2}(S'_{21}-S'_{12})-\omega)}{2(\alpha_oa^2+\beta_ob^2)\gamma_o}\\
E_1&=-\frac{\frac{1}{2}(S'_{12}+S'_{21})}{\gamma_o},\\
F_1&=\frac{S'_{11}(a^2+b^2)}{(\alpha_o+\beta_o)-(a^2+b^2)\gamma_o}
\end{aligned}\right] \quad \text{(A8)}$$

It may be noted that the expressions of constants, C_1, D_1, E_1 are identical to that of H, H', T (Eqs. 26 and 27) of Jeffery. Substituting $\lambda=0$ in Eqs. (A4)–(A6), we get:

$$\alpha_o=\frac{2}{a(a+b)},$$
$$\beta_o=\frac{2}{b(a+b)} \text{ and } \gamma_o=\frac{2}{ab(a+b)^2}. \quad \text{(A9)}$$

From Eq. (37) of Jeffery (1922) we can get,

$$\omega=\frac{a^2S'_{21}-b^2S'_{12}}{a^2+b^2} \quad \text{(A10)}$$

The constants in Eq. (A8) are now obtained in terms of known quantities, after substituting them in Eqs. (A1a) and (A1b) and some algebra we can have the expressions of the velocity functions in Eqs. (5a) and (5b).

References

Bell, T.H., 1985. Deformation partitioning and porphyroblast rotation in metamorphic rocks: a radical interpretation. J. Metamorph. Geol. 3, 109–118.

Bell, T.H., Rubenach, M.J., 1980. Crenulation cleavage development — evidence for progressive, bulk inhomogeneous shortening from millipede microstructures in the Robertson Metamorphics. Tectonophysics 68, T9–T15.

Bjornerud, M., 1989. Mathematical model for folding of layering near rigid objects in shear deformation. J. Struct. Geol. 11, 245–254.

Bjornerud, M.G., Zhang, H., 1995. Flow mixing object matrix

coherent mantle growth and the development of porphyroclast tails. J. Struct. Geol. 17, 1347–1350.

Ghosh, S.K., 1975. Distortion of planar structures around rigid spherical bodies. Tectonophysics 28, 185–208.

Ghosh, S.K., Ramberg, H., 1976. Reorientation of inclusions by combination of pure shear and simple shear. Tectonophysics 34, 1–70.

Hanmer, S., 1990. Natural rotated inclusions in non-ideal shear. Tectonophysics 176, 245–255.

Ildefonse, B., Mancktelow, N.S., 1993. Deformation around rigid particle: influence of slip at the particle/matrix interface. Tectonophysics 221, 345–359.

Jeffery, G.B., 1922. The motion of ellipsoidal particles immersed in a viscous fluid. Proc. R. Soc. Lond., A (120), 161–179.

Jezek, J., Saic, S., Segeth, K., Schulmann, K., 1999. Three-dimensional hydrodynamical modelling of viscous flow around a rotating ellipsoidal inclusion. Comput. Geosci. 25, 547–558.

Johnson, S.E., Bell, T.H., 1996. How useful are millipede and other similar porphyroblast microstructures for determining synmetamorphic deformation histories? J. Metamorph. Geol. 14, 15–28.

Lamb, H., 1932. Hydrodynamics. Cambridge University Press, Cambridge, 738 pp.

Mandal, N., Chakraborty, C., 1990. Strain fields and foliation trajectories around pre-, syn- and post-tectonic plutons in coaxially deformed terrains. Geol. J. 25, 19–33.

Mandal, N., Samanta, S.K., Chakraborty, C., 2000. Progressive development of mantle structures around elongate porphyroclasts: insights from numerical models. J. Struct. Geol. 22, 993–1008.

Masuda, T., Ando, S., 1988. Viscous flow around a rigid spherical body: a hydrodynamical approach. Tectonophysics 148, 337–346.

Masuda, T., Mizuno, N., 1996a. Deflection of non-Newtonian simple shear flow around a rigid cylindrical body by the finite element method. J. Struct. Geol. 18, 1089–1100.

Masuda, T., Mizuno, N., 1996b. Computer modeling mantled porphyroclasts in Newtonian and non-Newtonian simple shear viscous flows. J. Struct. Geol. 18, 1487–1491.

Masuda, T., Mochizuki, S., 1989. Development of snowball structures: numerical simulation of inclusion trails during synkinematic porphyroblast growth in metamorphic rocks. Tectonophysics 170, 141–150.

Passchier, C.W., 1994. Mixing in flow perturbations: a model for development of mantle porphyroclasts in mylonites. J. Struct. Geol. 16, 733–736.

Passchier, C.W., Simpson, S., 1986. Porphyroclast systems as kinematic indicators. J. Struct. Geol. 8, 831–844.

Pennacchioni, G.P., Fasolo, L., Cecchi, M.M., Salasnich, L., 2000. Finite-element modelling of simple shear flow in Newtonian and non-Newtonian fluids around circular rigid particle. J. Struct. Geol. 22, 683–692.

Ramberg, H., 1975. Particle paths, displacement and progressive strain applicable to rocks. Tectonophysics 28, 1–37.

Ramsay, J.G., Huber, M.I., 1987. The Techniques of Modern Structural Geology, vol. 2. Academic Press, London.

Rosenfeld, J.L., 1970. Rotated garnets in metamorpic rocks. Geol. Soc. Am. Spec. Paper 129, 1.

Simpson, C., De Paor, D.G., 1993. Strain and kinematic analysis in general shear zones. J. Struct. Geol. 15, 1–20.

Simpson, C., Schmid, S.M., 1983. An evaluation of criteria to determine the sense of movement in sheared rocks. Bull. Geol. Soc. Am. 94, 1281–1288.

Spry, A., 1969. Metmorphic Textures. Pergamon, New York.

ten Brink, C., Passchier, C.W., 1995. Modeling of mantled porphyroclasts using non-Newtonian rock analogue materials. J. Struct. Geol. 17, 131–146.

Van Den Driessche, J., Brun, J.P., 1987. Rolling structures at large shear strain. J. Struct. Geol. 9, 691–704.

Willis, D.G., 1977. A kinematic model of preferred orientation. Bull. Geol. Soc. Am. 88, 883–894.